Author for correspondence:
Andrea Kneib-Walter,
E-mail: andrea.walter@geo.uzh.ch

Observational constraints on the sensitivity of two calving glaciers to external forcings

Andrea Kneib-Walter[1,2] (iD), Martin P. Lüthi[1] (iD), Martin Funk[2],
Guillaume Jouvet[1] (iD) and Andreas Vieli[1]

[1]Institute of Geography, University of Zurich, Zurich, Switzerland and [2]Laboratory of Hydraulics, Hydrology and Glaciology, ETH Zurich, Zurich, Switzerland

Abstract

Future mass loss projections of the Greenland ice sheet require understanding of the processes at a glacier terminus, especially of iceberg calving. We present detailed and high-rate terrestrial radar interferometer observations of Eqip Sermia and Bowdoin Glacier, two outlet glaciers in Greenland with comparable dimensions and investigate iceberg calving, surface elevation, velocity, strain rates and their links to air temperature, tides and topography. The results reveal that the two glaciers exhibit very different flow and calving behaviour on different timescales. Ice flow driven by a steep surface slope with several topographic steps leads to high velocities, areas of extension and intense crevassing, which triggers frequent but small calving events independent of local velocity gradients. In contrast, ice flow under smooth surface slopes leaves the ice relatively intact, such that sporadic large-scale calving events dominate, which initiate in areas with high shearing. Flow acceleration caused by enhanced meltwater input and tidal velocity variations were observed for terminus sections close to floatation. Firmly grounded terminus sections showed no tidal signal and a weak short-term reaction to air temperature. These results demonstrate reaction timescales to external forcings from hours to months, which are, however, strongly dependent on local terminus geometry.

1. Introduction

Tidewater outlet glaciers in Greenland have accelerated, thinned and retreated strongly during the last decade (Rignot and Kanagaratnam, 2006; Howat and others, 2008; Moon and others, 2012; King and others, 2020). These glaciers are prone to be important for the future contribution of the Greenland ice sheet mass loss to sea level rise through ice discharge into the ocean (Enderlin and others, 2014; Van den Broeke and others, 2016; The IMBIE Team, 2020). For the ice discharge, processes at the calving front, especially iceberg calving, are key but observations with high temporal and spatial resolution are still rare. Such observations are needed to understand the link to external forcings and accurately resolve their sensitivity in future projections.

Observations show that the processes at the calving front can be very different and the intrinsic timescale strongly individual. Some glaciers show a clear diurnal variation in local stress conditions (Podolskiy and others, 2016; van Dongen and others, 2020), velocity (Davis and others, 2014; Kane and others, 2020) or calving activity (Minowa and others, 2019). These diurnal variations can be caused by tides (e.g. Voytenko and others, 2015; Cassotto and others, 2019; Seddik and others, 2019) or subglacial discharge (Podrasky and others, 2012). Falling tides result in reduced water pressure at the calving front causing extensional stress and higher velocities (Sugiyama and others, 2015; Podolskiy and others, 2016). Subglacial discharge can also lead to short-term speed-up events (Vieli and others, 2004; Sundal and others, 2013; Jouvet and others, 2018). Other studies found no relation between calving activity and tides or other short-term forcings (Walter and others, 2020; Cook and others, 2021). Several outlet glaciers in Greenland were observed to have a clear seasonal cycle with a related variation of calving over time controlled by bed topography, subglacial meltwater discharge, oceanic melt and the presence of ice melange (e.g. Howat and others, 2010; Fried and others, 2018; Xie and others, 2019; Cook and others, 2021; Kneib-Walter and others, 2021). For these observed controlling processes the fjord depth in front of the glacier was suggested to be an important control, especially for the ocean circulation (Sakakibara and Sugiyama, 2020). The seasonal cycle is observed to be spatially and temporally variable for individual glaciers (Schild and Hamilton, 2013). Overall, the sensitivity of each glacier to external forcings varies strongly, and understanding the mechanisms and interactions between the different characteristics is thus essential to understand why some glaciers are more sensitive than others.

Observation techniques with high temporal and spatial resolution are necessary to observe the processes at the calving front in detail. An increasingly used technique to investigate short timescale processes is terrestrial radar interferometry (TRI; e.g. Voytenko and others, 2015; Lüthi and Vieli, 2016; Xie and others, 2018, 2019; Cassotto and others, 2019; Cook and others, 2021). This technique can overcome temporal restrictions of other methods and enables measuring calving event sizes, flow velocities and surface topography directly and at very high rate.

So far, TRI data were used to study individual glaciers and specific processes, but there exist no direct glacier-to-glacier comparisons using the same observation technique, namely TRI, to safely avoid biases due to differences in measurement techniques.

Here, we analyse the dynamics and calving activity of two tidewater outlet glaciers of the Greenland ice sheet using TRI data recorded during two field campaigns, and perform a comparative analysis. Such a comparison allows us to gain new insights into the wide range of calving processes. The two glaciers of similar size investigated in this study show very different characteristics, and therefore cover a wide range of possible glacier terminus processes which are representative for most smaller tidewater glaciers in Greenland. Our dataset covers a wide range of different front geometries, flow dynamics and calving activity. This enables us to analyse the different front characteristics over time and space and to investigate their sensitivity to tides, air temperature, bathymetry and changing seasonal forcings. This allows us to investigate the influence of environmental conditions and geometrical settings, and to compare the magnitude and the intrinsic timescale of the reactions of those contrasting glaciers to external forcings.

2. Study areas and data acquisition methods

2.1 Study areas

Two ocean terminating outlet glaciers located at the western and north-western margin of the Greenland ice sheet, respectively, with differing front geometry and dynamics were studied during two field seasons (Fig. 1).

Eqip Sermia (69.81° N, 50.20° W), a grounded outlet glacier in West Greenland, has currently a width of ~3.2 km, a height above waterline between 50 and 170 m and flows with velocities up to 16 m d^{-1}. The glacier front terminates in a fjord with differing water depths along the front between 0 and 100 m (Rignot and others, 2015; Fig. 10 in Lüthi and others, 2016; Fig. 10 in Kneib-Walter and others, 2021). As in Walter and others (2020), the differing water depths were used to divide the glacier in three sectors with diverse front geometry and dynamics. The northern shallow sector (S, 0–20 m water depth) is characterised by a high, inclined front, while the southern deep sector

(D, 70–100 m water depth) shows a vertical front of lower cliff height. In between these two sectors the middle sector (M) is located where a rock ridge appears (Walter and others, 2020).

Bowdoin Glacier (77.41° N, 68.35° W) is located in north-western Greenland. The glacier front with a width of 3 km was flowing at ~1.5 m d^{-1} around 2015 and 2017. The glacier was grounded in 2013, but near the floatation condition, with a total frontal thickness up to 250 m (Sugiyama and others, 2015). Since then further thinning and ungrounding of the terminus are likely (Van Dongen and others, 2021). The water depth close to the terminus is more than 100 m at the margins with a depression of ~250 m water depth towards the middle of the calving front (Fig. 4 in Sugiyama and others, 2015; Fig. 6 in Jouvet and others, 2017). After a rapid retreat in 2008, the front stabilised in 2013 at its current position (Sugiyama and others, 2015) but has been thinning at a rate of ~5 m a^{-1} (Tsutaki and others, 2016; Sakakibara and Sugiyama, 2018). The glacier can be separated into three sectors due to their velocity and the geometry of the front. While the northern (faster flowing, subsequently termed 'FF') and the middle sector (M) have a velocity of up to 1.5 m d^{-1} at the terminus, in the southern sector (slower flowing, subsequently termed 'SF') the velocity is almost stagnant and lower towards the lateral margin. The latter sector shows a higher front above the waterline than the northern sector. The middle sector features a ~25 m wide moraine without any crevasses forming a depression on the glacier surface. On the moraine meltwater in a stream flows down towards the glacier front (van Dongen and others, 2020). Several large-scale calving events were observed at this glacier and investigated in other studies with different observational methods (Jouvet and others, 2017; van Dongen and others, 2020, 2021).

2.2 Observational approach to calving activity, front geometry and flow dynamics

At Eqip Sermia and Bowdoin Glacier a terrestrial radar interferometer (TRI, Gamma GPRI) was installed on bedrock 150 and 495 m above sea level, respectively, with power supplied from a generator. The distance to the calving front was 4.5 km at Eqip Sermia (Figs 1a, 2a) and 3 km at Bowdoin Glacier (Figs 1b, 2b).
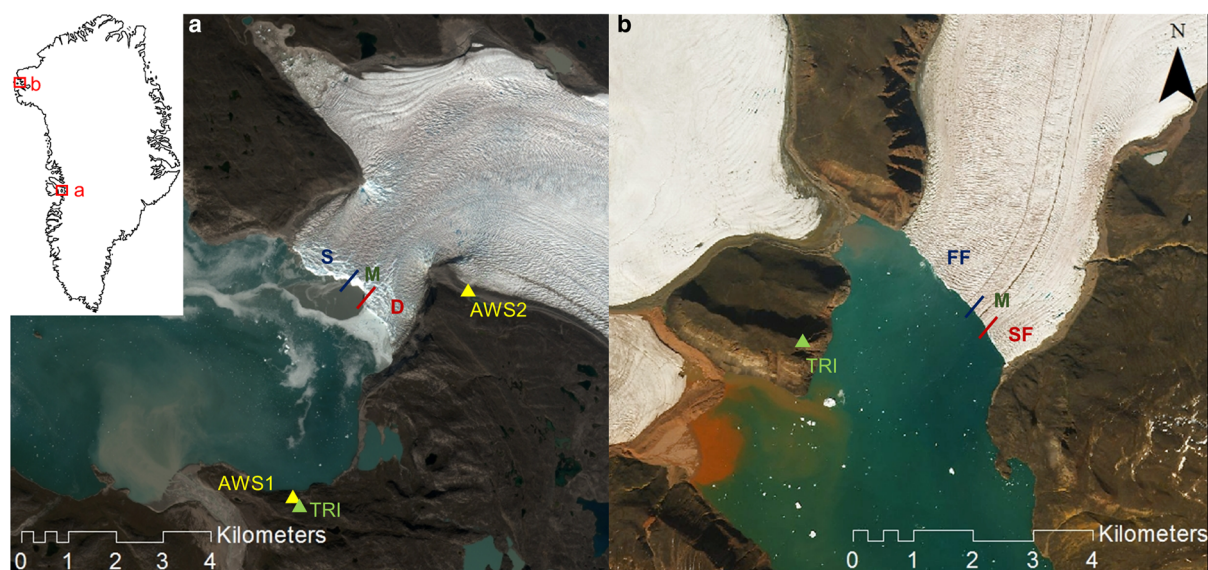

Fig. 1. Overview of Eqip Sermia and Bowdoin Glacier. (a) Eqip Sermia is divided into a shallow (S), a middle (M) and a deep sector (D) as the differing water depth is a striking feature for this glacier. Similarly, (b) Bowdoin Glacier is divided into a fast flowing (FF), a middle (M) and a slow flowing sector (SF) as for this glacier the different velocity is a striking feature. The positions of the TRI and the two AWSs are indicated by triangles. Background: Sentinel-2A scene from (a) 3 August 2016 for Eqip Sermia and (b) 25 July 2017 for Bowdoin Glacier (from ESA Copernicus Science Hub: https://scihub.copernicus.eu).
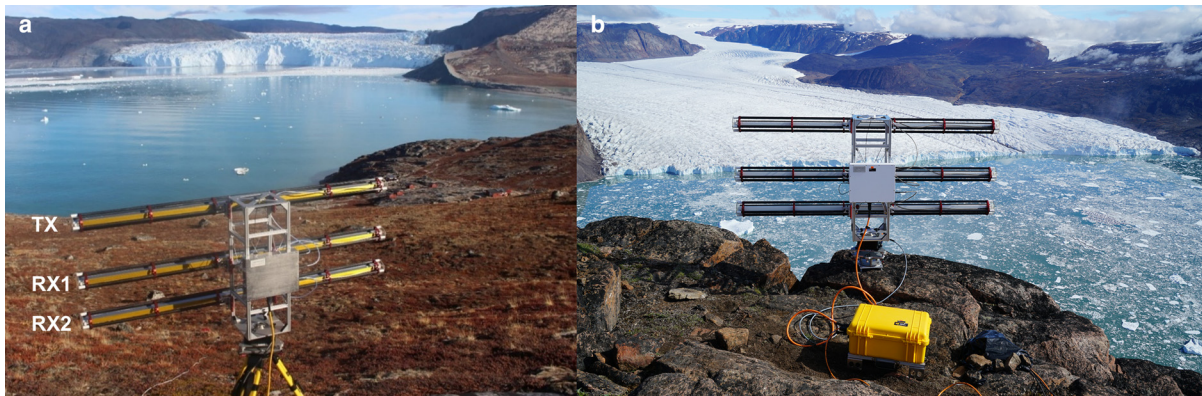
Fig. 2. The TRI with one transmitting (TX) and two receiving antennas (RX1, RX2) is located opposite of (a) the front of Eqip Sermia at a distance of 4.5 km and (b) at Bowdoin Glacier at a distance of 3 km.

In 2016, the TRI was measuring between 19 and 27 August at Eqip Sermia and between 7 and 19 July at Bowdoin Glacier. In 2017, it was recording between 16 and 25 June at Eqip Sermia and at Bowdoin Glacier between 4 and 16 July (Table 1). At Eqip Sermia the measurements were repeated at 1 min intervals in both years, while at Bowdoin Glacier the measurements intervals were 2 min in 2016 and 1 min in 2017. With these radar measurements an almost continuous record of velocity and surface elevation data was generated for the frontal area of Eqip Sermia and Bowdoin Glacier.

The Gamma GPRI is a real-aperture radar interferometer operating at a wavelength of $\lambda = 17.4$ mm (Ku-band, 17.2 GHz) and uses one transmitting and two receiving antennas. With the measurement surface elevation models and velocities in the line-of-sight of the TRI can be calculated. For the surface elevation models the interferograms between the two receiving antennas at the same time and for the velocity the interferograms with two consecutive images of one receiving antenna are used. The resolution is ∼0.75 m in range and 0.1° in azimuth corresponding to 7 m at a slant range of 1 km (Werner and others, 2008a).

2.3 Weather and ocean data

Two automatic weather stations (AWSs) collected hourly data at Eqip Sermia at the sites indicated in Figure 1. AWS1 installed near the TRI at 60 m a.s.l. was measuring in between July and December 2016 and in 2017 from mid-June onwards and was fully covering the field observation periods. The measured parameters are air temperature, relative humidity, wind speed and direction, incoming shortwave radiation and precipitation. AWS2 located next to the ice edge at 362 m a.s.l. measured air temperature, radiation and wind speed and direction during the field campaign 2016 and then from September onwards continuously. AWS2 is considered to be more representative for the meteorological conditions at the glacier due to the proximity to the ice sheet, whereas AWS1 represents the climate conditions at the shore of the fjord.

For the environmental conditions at Bowdoin Glacier the air temperature data of a weather station at Qaanaaq Airport (16 m a.s.l.) ∼30 km southwest of Bowdoin Glacier provided by the National Oceanic and Atmospheric Administration are used (http://www.ncdc.noaa.gov/cdo-web/datasets).

Pressure sensors were installed in the fjord water at the shore 4.5 km opposite of Eqip Sermia with a sampling rate of 2 s (Walter and others, 2020). The data obtained by these pressure sensors are used to extract the tides at the fjord in front of the glacier. To investigate the tides as potential forcings at Bowdoin Glacier, data measured at Thule Air Base from the Global Sea Level Observing System network (www.gloss-sealevel.org) were analysed. Thule Air Base is located 125 km south of Bowdoin Glacier, but shows comparable tidal records (Podolskiy and others, 2016).

3. Data processing methods

3.1 TRI data processing

The radar images measured with the TRI are used to calculate the velocity field for both glaciers. In a first step the interferograms between consecutive radar images from the same receiving antenna were calculated. A stacking of the interferograms over 1 h for Eqip Sermia and 2 h for Bowdoin Glacier before unwrapping the interferograms was used to reduce noise, which was mainly caused by phase shifts in the interferograms due to changes in air temperature, humidity and air pressure (Goldstein, 1995). The line-of-sight displacement was then calculated with the unwrapped interferograms (Werner and others, 2008b). Beside the velocity maps the displacement was extracted along three flowlines to investigate the difference between the two glaciers and the two field campaigns. To analyse the temporal variation the velocities were extracted at six points along the front and investigated over time.

The resulting velocity fields were further used to calculate the velocity gradient along the line-of-site direction (approximately the flow direction of the glacier). For this the difference in velocity from one pixel to the next in the direction of the radar beam was calculated. Positive values refer to increasing velocities and hence extension and negative values to compression. To obtain a general pattern of the velocity gradient and reduce noise the velocity gradient maps were further smoothed with a Gaussian filter with a std dev. sigma of 0.8. The final velocity gradients were analysed as spatial maps and for six points along the front over time. Additionally, the velocity gradient was extracted along the front
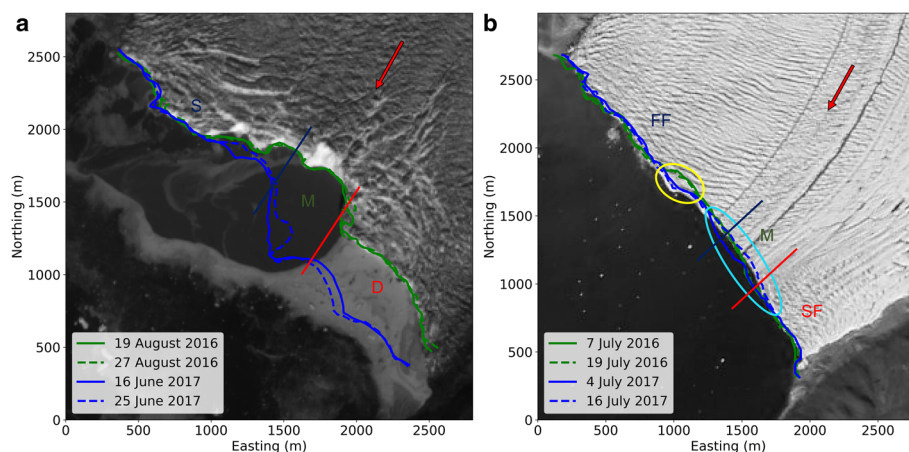
Table 1. Field campaigns dates, duration and state in the melt season at Eqip Sermia and Bowdoin Glacier. The state in the melt season was concluded considering air temperatures (Figs S3, S4) and Sentinel-2A images (from ESA Copernicus Science Hub: https://scihub.copernicus.eu).

Field campaign	Eqip Sermia 2016	Eqip Sermia 2017	Bowdoin 2016	Bowdoin 2017
Dates	19–27 August	16–25 June	7–19 July	4–16 July
Duration (d)	7.5	9.5	12	12
State in melt season	Late melt season	Early melt season	Middle melt season	Early melt season

Fig. 3. Position of the front (a) of Eqip Sermia and of (b) Bowdoin Glacier at the beginning and the end of the TRI observation in 2016 and 2017. The red arrow represents the main flow direction of the glaciers. The different sectors of the fronts are marked with lines and in (b) the two parts where the front position changed are marked yellow and light blue. Background: Sentinel-2A scene from (a) 3 August 2016 and (b) 25 July 2017 (from ESA Copernicus Science Hub: https://scihub.copernicus.eu).

line to further investigate relationships with environmental forcing and calving. The front line was drawn manually and changed over time with the retreat and advance of the glaciers.

As the TRI receives the radar signal with two antennas RX1 and RX2, a reconstruction of the topography at a high temporal resolution can be achieved. For this purpose interferograms between RX1 and RX2 are calculated and unwrapped following the standard workflow of Caduff and others (2015). The unwrapped phases were then converted to topography (Strozzi and others, 2012) and corrected for systematic errors (Walter and others, 2020). The resulting DEMs are then stacked over 10 min to reduce noise. Similarly to velocity, the surface elevation values were extracted along three flowlines.

The DEMs were further used to quantify calving events following the method described in Walter and others (2020). By subtracting the consecutive DEMs negative height changes can be located and using several thresholds be extracted. The extraction thresholds are needed to reduce noise and increase the signal-to-noise ratio on stable terrain. The thresholds consider a minimal height change (>5 m), a minimal area of 10 pixels and a minimal width larger than 3 pixels (11.25 m). Additionally, the calving events need to fulfil a shape condition if they are smaller than 40 pixels ((number of pixels × 1.6) ≥ (number of pixels in bounding box)). Due to the stacking of the DEMs calving events within 10 min are merged. A mask at the glacier front as a line with a buffer of ∼75 m on each side was used to exclude icebergs in the fjord and collapsing seracs upstream the glacier.

The calculations are all done in the radar geometry and only for the velocity, velocity gradient and surface elevation maps the final results were reprojected into the Cartesian UTM22N grid. This ensures that projection errors do not influence the calculations and the final results.

The TRI data were additionally used to investigate the emergence of subglacial meltwater plumes at the calving front. On the multi-look images the footprint of a subglacial meltwater plume is well discernible if the fjord is covered with thin ice melange. The findings were further validated with observations in the field and Sentinel-2 images (from ESA Copernicus Science Hub: https://scihub.copernicus.eu).

3.2 Tides

At Eqip Sermia the pressure sensor data from the tide gauges in the fjord were converted to water height. Using a low-pass filter with a pass frequency of 0.001 Hz, the tidal amplitudes (Fig. S5) and timing of rising tides were then extracted and analysed regarding potential forcings for the glacier dynamics.

4. Results

4.1 Calving front position and surface elevation

The positions of the front at the beginning and the end of the TRI observations in 2016 and 2017 are shown in Figure 3 for Eqip Sermia and Bowdoin Glacier. While at Bowdoin Glacier the calving front positions were similar for both field campaigns, this was only the case for the northern part of Eqip Sermia, whereas the middle and southern parts differed substantially. The calving front elevations along the front of Eqip Sermia amount to 30–175 m (Table 2, Fig. 5b) but are with 15–45 m substantially lower at Bowdoin Glacier (Table 2, Fig. 6b). The spatial variations along the front were higher for Eqip Sermia due to the strongly crevassed surface. While at Bowdoin Glacier the difference of surface elevation between the two campaigns was <15 m, this difference reached up to 75 m for Eqip Sermia.

4.1.1 Eqip Sermia

During the field season 2016, which took place late in the melt season, the calving front position was in a stable retreated position (Fig. 3a). In contrast, during the early melt season campaign in 2017 the front was in an advanced position with lower surface elevations and small retreats in sectors M and D. Figure 7a shows the surface elevation along three flowlines at the beginning and the end of the observation period. Also here the elevation differences and front slopes were larger in sectors M and D. The results obtained at different states in the seasonal cycle give an indication of the high variation throughout the year.

4.1.2 Bowdoin Glacier

The front position was stable during the 2016 field campaign, while in 2017 the front retreated in sector M (marked light blue in Fig. 3b). The results of two field campaigns obtained during climatically very different years indicate that the variations throughout the year are marginal. The surface elevation of the front was similar during both years ∼30 m a.s.l. in sector FF, 20 m a.s.l. in

Table 2. Characteristics of Eqip Sermia and Bowdoin Glacier measured with the TRI during the field campaigns 2016 and 2017 showing the main differences (water depths from Lüthi and others, 2016; Jouvet and others, 2017)

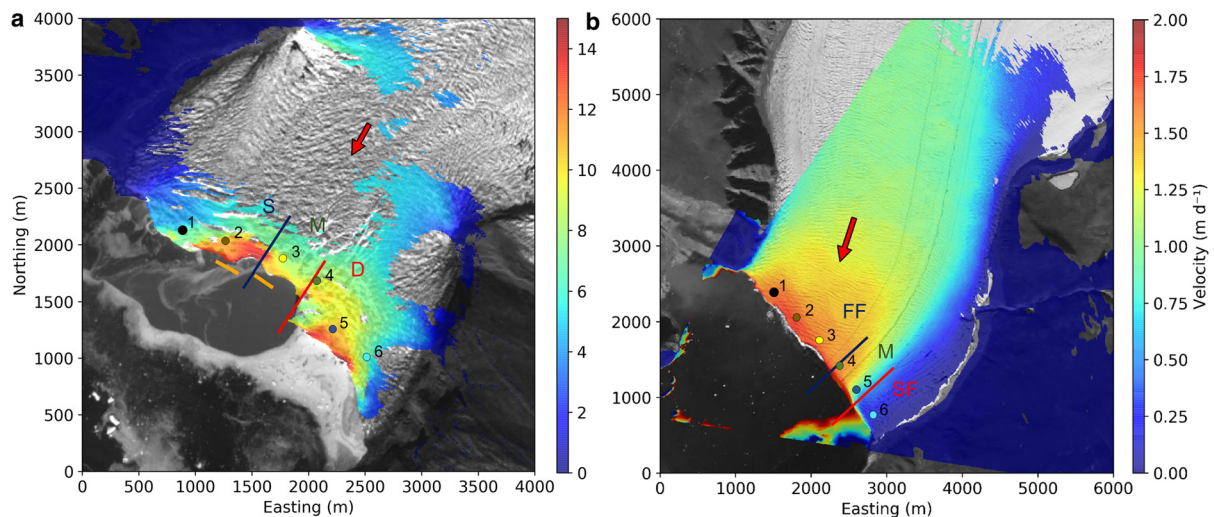|	Eqip Sermia	Bowdoin Glacier
Front width (m)	3200	3000
Max/min front height	175/33	44/14
Max/min water depth at front (m)	100/0	250/100
Max velocity at front (m d^{-1})	12	1.5
Max/min velocity gradient at front (10^{-2} d^{-1})	22/−29	3.3/−1.6
Calving rate 2016/2017 (10^6 m^3 d^{-1})	2.6/2	0.02/0.09

Fig. 4. Velocity maps inferred from TRI data of (a) Eqip Sermia and (b) Bowdoin Glacier. The red arrow indicates the flow direction of the glacier. The velocity at points 1–6 are plotted over time in Figures 11 and 12. The different sectors of the fronts are marked with lines. The orange horizontal bars in (a) correspond to bedrock visible above the waterline. Background: Sentinel-2A scene from (a) 3 August 2016 and (b) 25 July 2017 (from ESA Copernicus Science Hub: https://scihub.copernicus.eu).

sector M and 40 m a.s.l. in sector SF (Fig. 7b). In parts of sectors FF and M (circled areas in Fig. 3b) the front was higher and more retreated in 2016 (Fig. 6b). A large calving event was observed in 2017 in sector M. Upstream of the glacier front the surface elevation increased from 2016 to 2017 by ~10–15 m (Fig. 7c), which is likely an effect of surface mass balance and related changes in ice discharge.

4.2 Flow velocity

The flow velocities determined with the TRI are shown in Figures 4–8. In general Eqip Sermia accelerates rapidly towards the front with two areas of high speed of 12 m d^{-1} (Fig. 4a) due to the steepness of its topography. In contrast, the velocities for Bowdoin Glacier are an order of magnitude lower with maximum values of 1.5 m d^{-1} and they show much less acceleration towards the front. The velocity along the front also was more homogeneous for Bowdoin Glacier than at Eqip Sermia, with an almost stagnant sector SF at the left margin.

4.2.1 Eqip Sermia

The velocity along the front was similar in both years in sector S (Fig. 5a), but differed considerably in sectors M and D. While sector M and the northern half of sector D moved faster in 2016, the southern half of sector D was slower. Figure 8a shows the velocity along three flowlines with large differences in sectors M and D. Sector S showed little change in both flow speed and surface geometry between the two years (Fig. 7a) whereas in sectors M and D velocities are substantially lower in 2017 alongside a more advanced position of the front. In Figures 11a and b the velocity at six points along the front over time indicates only small variations for both years. A relation to air temperature and tides is only observable when subtracting the mean velocity (Fig. S2). Increasing temperatures cause in many occasions a slight acceleration. In 2017 points 5 and 6 reach their highest speed slightly before the tide rate peaks (Fig. S2). This positive correlation (Pearson) is found to be more significant when adding a time lag (highest velocity slightly before highest tide rate). No clear patterns in short-term flow speed variations were observed
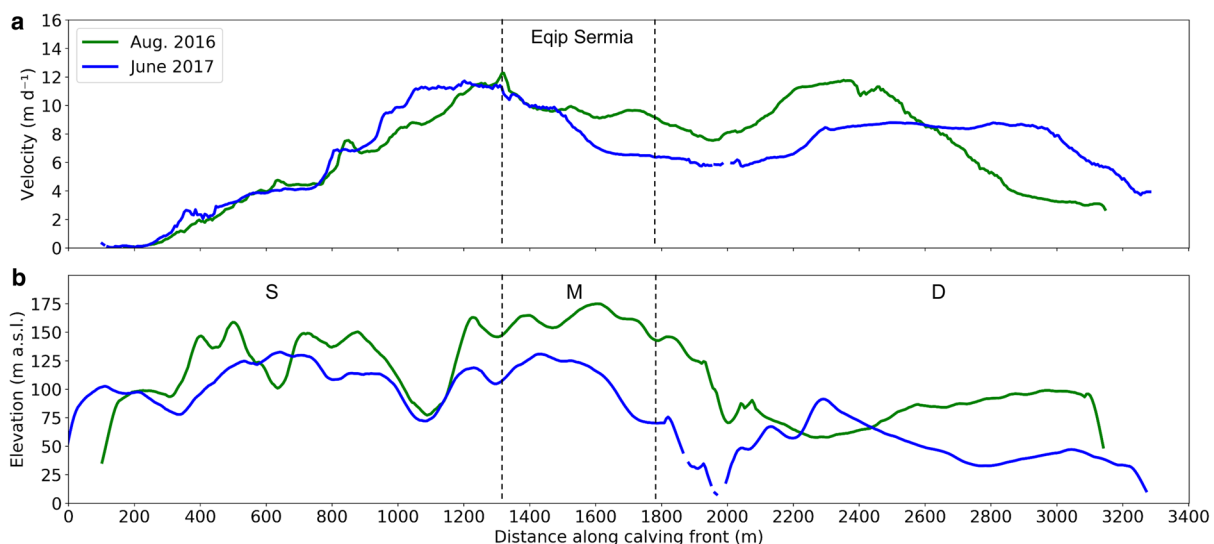

Fig. 5. (a) Velocity and (b) surface elevation of Eqip Sermia along the front for the field campaigns in 2016 and 2017. The three sectors shallow (S), middle (M) and deep (D) are separated with vertical black lines.
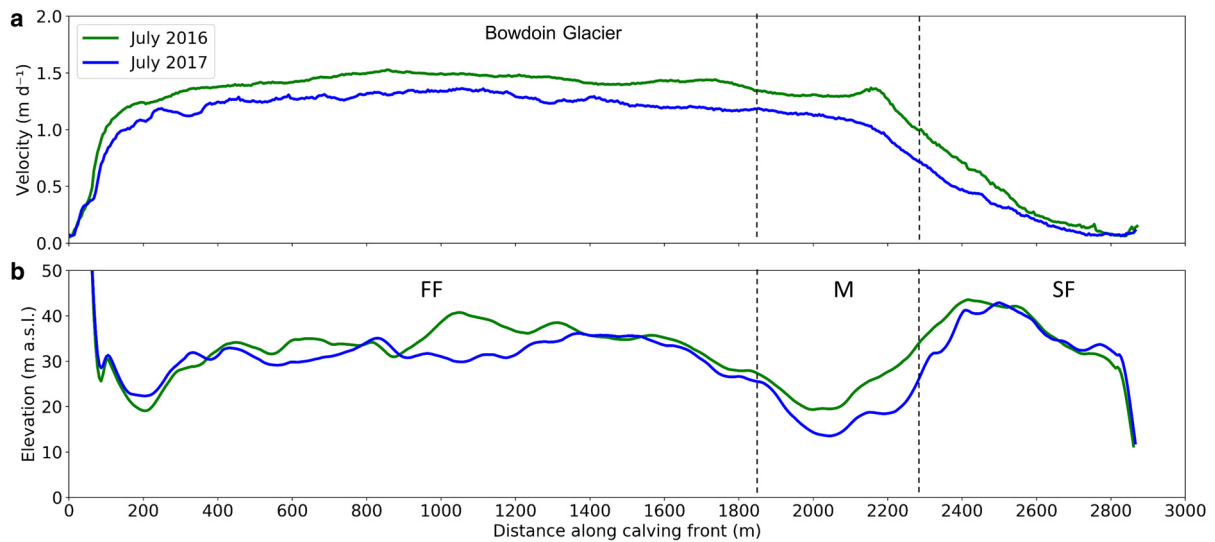
Fig. 6. (a) Velocities and (b) surface elevation for Bowdoin Glacier along the front for the field campaigns in 2016 and 2017. The three sectors fast flowing (FF), middle (M) and slow flowing (SF) are separated with vertical black lines.

despite large differences within the melt season as the two field campaigns early (2017) and late (2016) in the melt season show different flow velocities.

4.2.2 Bowdoin Glacier

The velocity along the front shows the same pattern for both years but with generally slightly lower velocities (15%) in 2017 (Fig. 6a). The velocities along three flowlines show differences between the two years but also between the beginning and the end of the

observation periods (Fig. 8b). Sectors M and SF had a strongly increased velocity at the front at the beginning of the observation period before a large calving event on 8 July in 2017 (black dotted boxes in Fig. 8b). In Figures 12a and b the velocities at six points along the front increase in 2016 at the beginning of the field season with a peak around midnight of 8/9 July and a subsequent general decrease. A relation between flow velocity and tide rate is clearly visible in Figures 12a and b with highest velocities at decreasing tides. The observed negative Pearson correlation
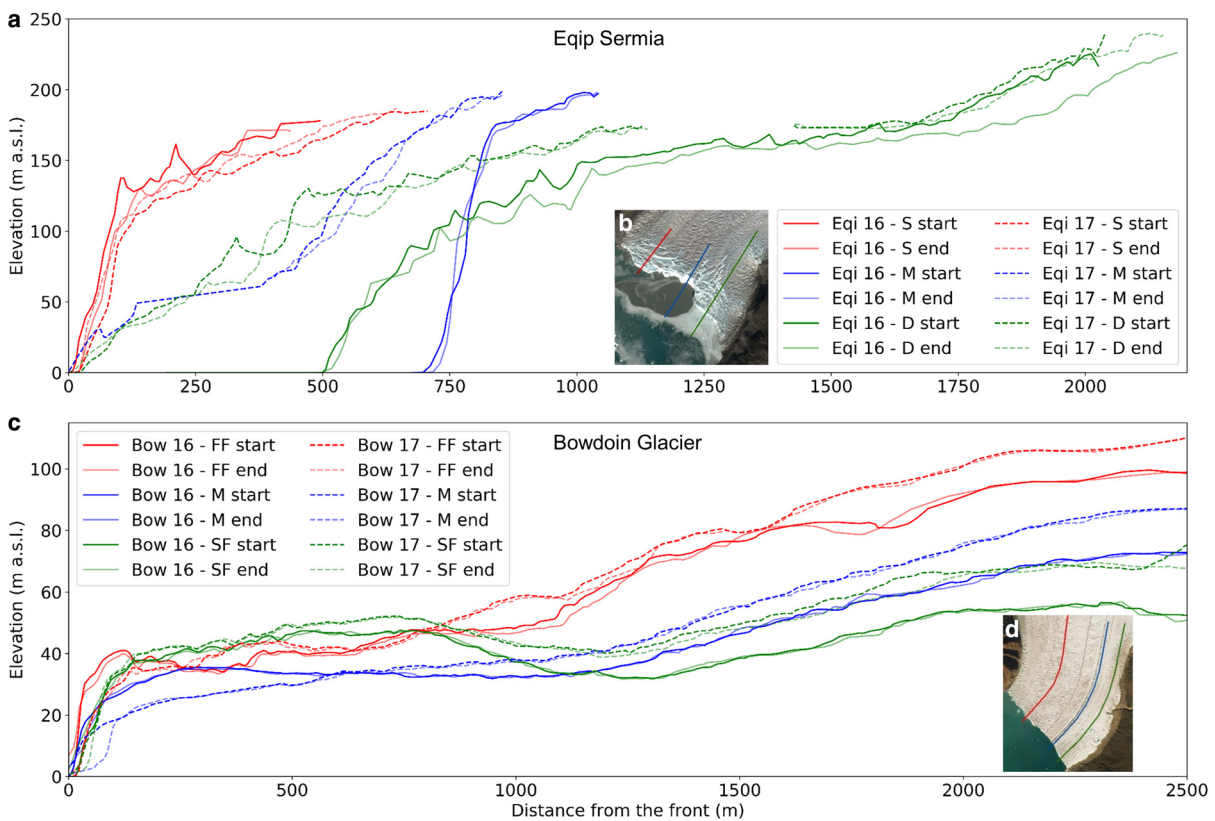

Fig. 7. Surface elevation along three flowlines of (a) Eqip Sermia and (c) Bowdoin Glacier for the beginning and the end of the observation period. (b) The three flowlines at Eqip Sermia represent the shallow (S, red), middle (M, blue) and deep sector (D, green). (d) The three flowlines at Bowdoin Glacier stand for the fast flowing (FF, red), the middle (M, blue) and the slow flowing sector (SF, green). Background: Sentinel-2A scene from (b) 3 August 2016 and (d) 25 July 2017 (from ESA Copernicus Science Hub: https://scihub.copernicus.eu).
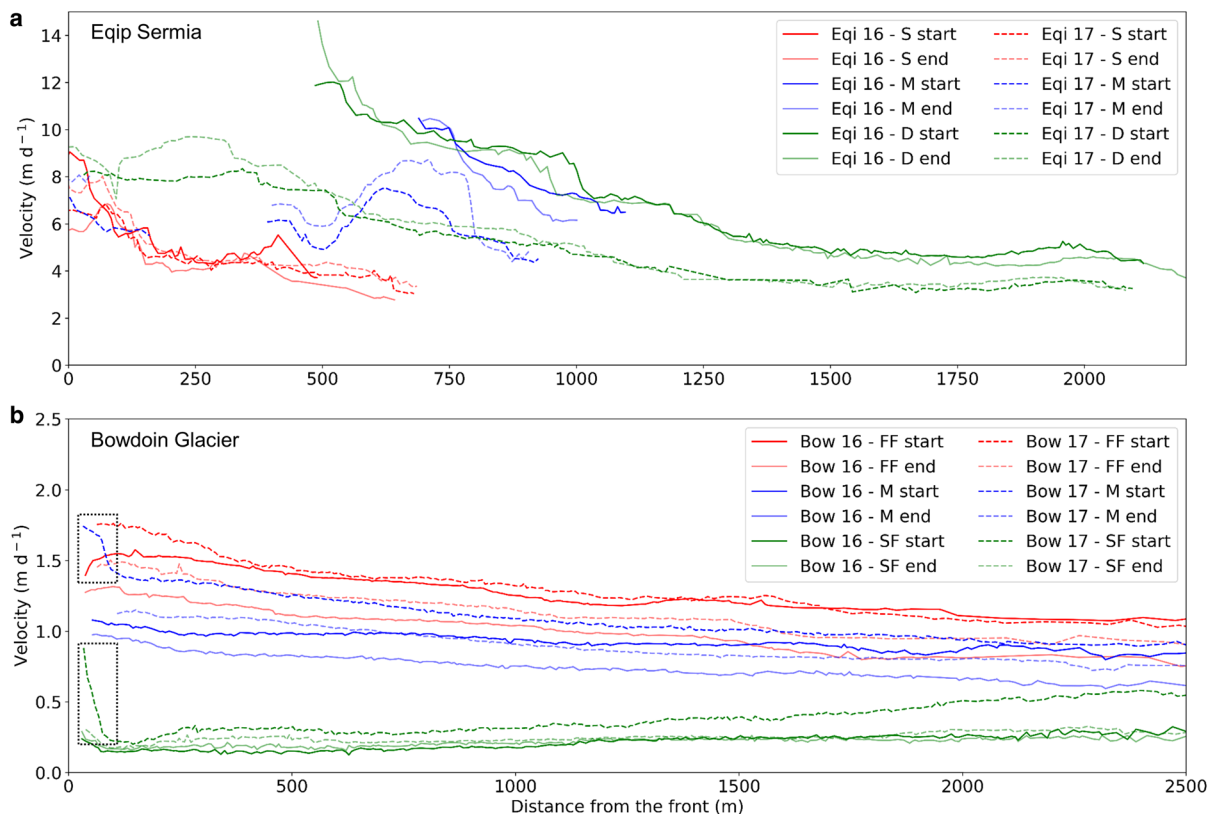
Fig. 8. Velocity along three flowlines of (a) Eqip Sermia and (c) Bowdoin Glacier for the beginning and the end of the observation period. The three flowlines at Eqip Sermia represent the shallow (S, red), middle (M, blue) and deep sector (D, green). The three flowlines at Bowdoin Glacier stand for the fast flowing (FF, red), the middle (M, blue) and the slow flowing sector (SF, green). For locations of the flowlines see Figure 7. The black dotted boxes indicate the increased velocities at the beginning of the field campaign 2017 for sectors M and SF.

between velocity and tide rate is significant ($p \leq 0.05$) for all six points except for points 2 and 3 in 2016. Strong short-term velocity variations (tidal and throughout several days) are characteristic for this glacier.

4.3 Velocity gradients

The velocity gradient maps calculated from TRI velocities in radar look direction (approximately the flow direction of the glacier) are shown in Figures 9 and 10. Positive values correspond to an increase in velocity (extension) and negative values to a slowdown. Due to the pronounced velocity variations, Eqip Sermia shows a more heterogeneous velocity gradient pattern than Bowdoin Glacier (Figs 9, 10). In Figures 13 and 14 the velocity gradient is shown as background together with colour-coded calving event volumes along the front over time. Higher velocity gradients were concentrated in several areas, whereby the location of these areas and the magnitude varied over time.

4.3.1 Eqip Sermia

The velocity gradient maps show several localised areas with positive values and hence extension (Fig. 9). These mostly narrow transvers bands of extension match the pattern of crevasses and rifts and hence likely causes the highly crevassed surface (Fig. S1a). A noteworthy feature is an area with negative values (green circle in Fig. 9d), which corresponds to the location of a large meltwater plume that emerged in 2016 when the front position had retreated to this area. Upstream and south of this region the surface is strongly crevassed and exhibits curved crevasse patterns (region C in Fig. S1a). The temporal evolution of the velocity gradient for six points along the front shows small variations except for position 2 in sector S with high variations

in 2016 and 2017 (Figs 11c, d). During the 2017 field campaign the velocity gradient along the front over time (Fig. 13) increases before several large calving events (on 18, 19, 22, 23 and 24 June) with an immediate drop afterwards.

4.3.2 Bowdoin Glacier

Extensional velocity gradients (Fig. 10b) are very localised towards the calving front and resemble the crevasse patterns in Figure S1b, which is likely a sign of crevasse opening. The low velocities in sector SF caused high positive velocity gradients in the area circled with blue in Figure 10a, indicating a lateral shear zone (Jouvet and others, 2017). In 2017 at the beginning of the observation period the velocity gradients were much higher than in 2016 or at the end of 2017 in the green circled area in sector M (Fig. 10b) and were related to rapid crevasse opening before the calving event (Figs 10b and d). With regards to tidal forcing, the influence on velocity gradients is apparent at all six points along the calving front, showing highest velocity at lowest tide rate (Figs 12c and d), whereby point 5 located between sectors M and SF shows anomalously high variations. Tidal variations are also reflected for the velocity gradient in Figure 14 as bands of enhanced extension as for example before the large calving event in 2017. An increase of the velocity gradient before the large calving event is followed by an immediate drop afterwards.

4.4 Calving activity and volumes

Calving events were detected with the TRI and the individual volumes calculated. In Figures 13 and 14 the colour-coded calving event volumes along the front over time are shown alongside the velocity gradients at the front. The results show that the calving
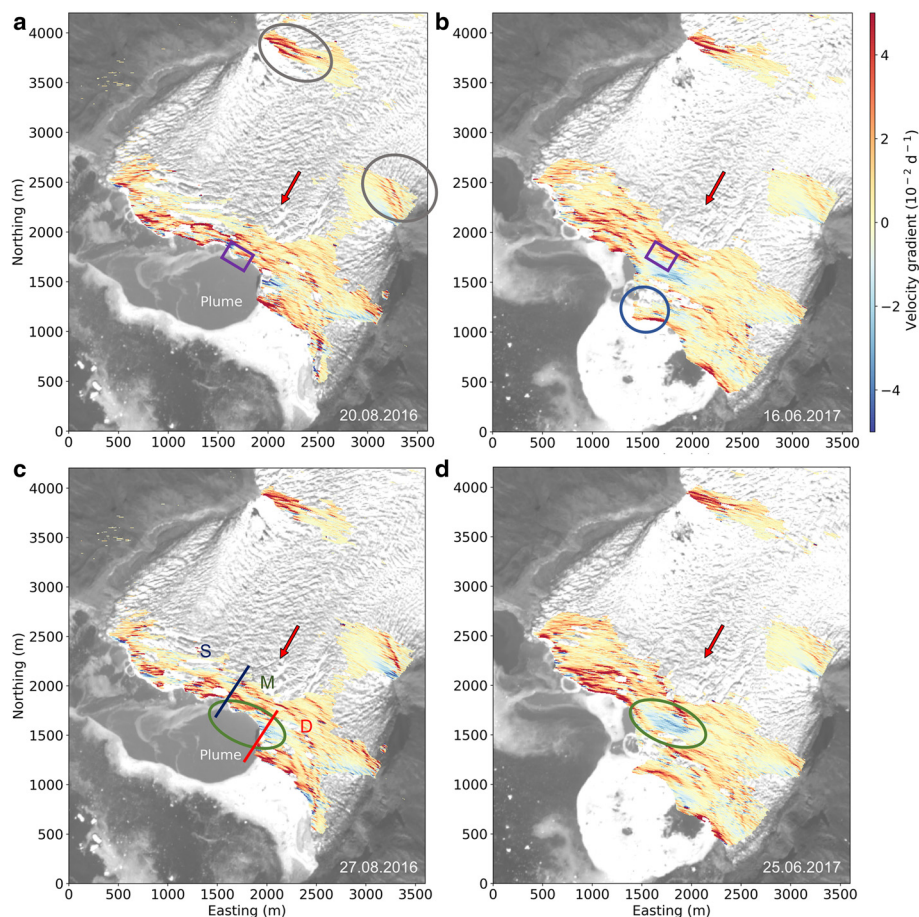
Fig. 9. Velocity gradient maps for Eqip Sermia (a) at the beginning and (c) at the end of the observation period in 2016 and (b) at the beginning and (d) at the end of the field campaign 2017. The square shows the same location for better orientation. The blue circle shows a spire, which retreated in 2016. The green circle shows a compression zone in 2017, while in 2016 the glacier already retreated behind this area. The different sectors of the fronts are marked with lines. The grey circles mark examples of topographical steps. Background: Sentinel-2A scene from 3 August 2016 (a and c) and 11 July 2017 (b and d) (from ESA Copernicus Science Hub: https://sci-hub.copernicus.eu).

activity and volumes are highly variable over time and space and substantially different for the two glaciers.

4.4.1 Eqip Sermia

The number of calving events per day in 2017 was with 107 substantially lower than for 2016 with 149 (Table 3). In the late field season 2016, the calving rates and volumes differed substantially for the three sectors with reduced calving activity in sector D. Large events only occurred in sector M, within the area of the subglacial meltwater plumes P2 and P3. The early field campaign 2017 showed an increasing calving activity towards the end of the campaign. Large events occurred in the areas influenced by the subglacial meltwater plumes P2 and P4. A concentrated occurrence of events in sector D was observed at a protruding ice spire (indicated in blue in Fig. 9b), which was in a retreated position in 2016. The results show a clear difference between observations during different states in the seasonal cycle but no clear short-term forcing (Fig. 13).

4.4.2 Bowdoin Glacier

For the field campaign 2016 almost four times more events per day were detected than in 2017. The events in 2016 were rather small with a maximum volume of 28 300 m^3, while in 2017 one large event of 844 000 m^3 on 8 July dominated the observations. This event was related to a full thickness calving event (Van Dongen and others, 2020), but the TRI can only measure calving volumes above the waterline. Assuming a mean water depth of 210 m (Jouvet and others, 2017) at this location and a full-thickness calving event, the size of the event below the waterline can be estimated as 11 800 000 m^3, resulting in a total volume of 12 644 000 m^3. This event in sector M at the middle moraine was initiated by a large and rapidly opening crevasse (Fig. 10b)

and an acceleration before break-off (Fig 6 in Van Dongen and others, 2020) which is also well visible in Figure 14d by the increase of the velocity gradient. At this location, meltwater plume P2 disappeared after the calving event and reappeared after several days.

5. Discussion

The results of this study show that two glaciers of similar size exhibit substantially different reactions on different timescales, even if the forcings are similar. On short timescales (minutes to hours) a reaction to external forcings like tides and air temperatures can occur, while on long timescales (seasonal) the glacier geometry and stress conditions are influenced by topography, subglacial meltwater discharge and ice melange. Even within one glacier terminus different sectors can be isolated based on their dynamics, seasonal evolution and calving pattern. Analysing this wide variety of behaviours and linking it to geometrical and ice-dynamical characteristics is one of the key aspects of this study.

Our study draws from observational results acquired on Eqip Sermia and Bowdoin Glacier, which differ essentially regarding their geometries, flow patterns and calving activity (Table 2). Together they cover a wide variety of calving front characteristics. The flow of Eqip Sermia is driven by a steep surface slope including several topographical steps with high flow velocities and terminates in a fjord that is partly very shallow. Consequently, the velocity gradient pattern is heterogeneous with many areas of extension reflecting, and likely causing, the highly crevassed surface (Fig. 9). Hence, the inclined and high front is calving continuously (Fig. 13). In contrast, Bowdoin Glacier has a uniform gentle slope, flows at lower velocity, and terminates in deeper
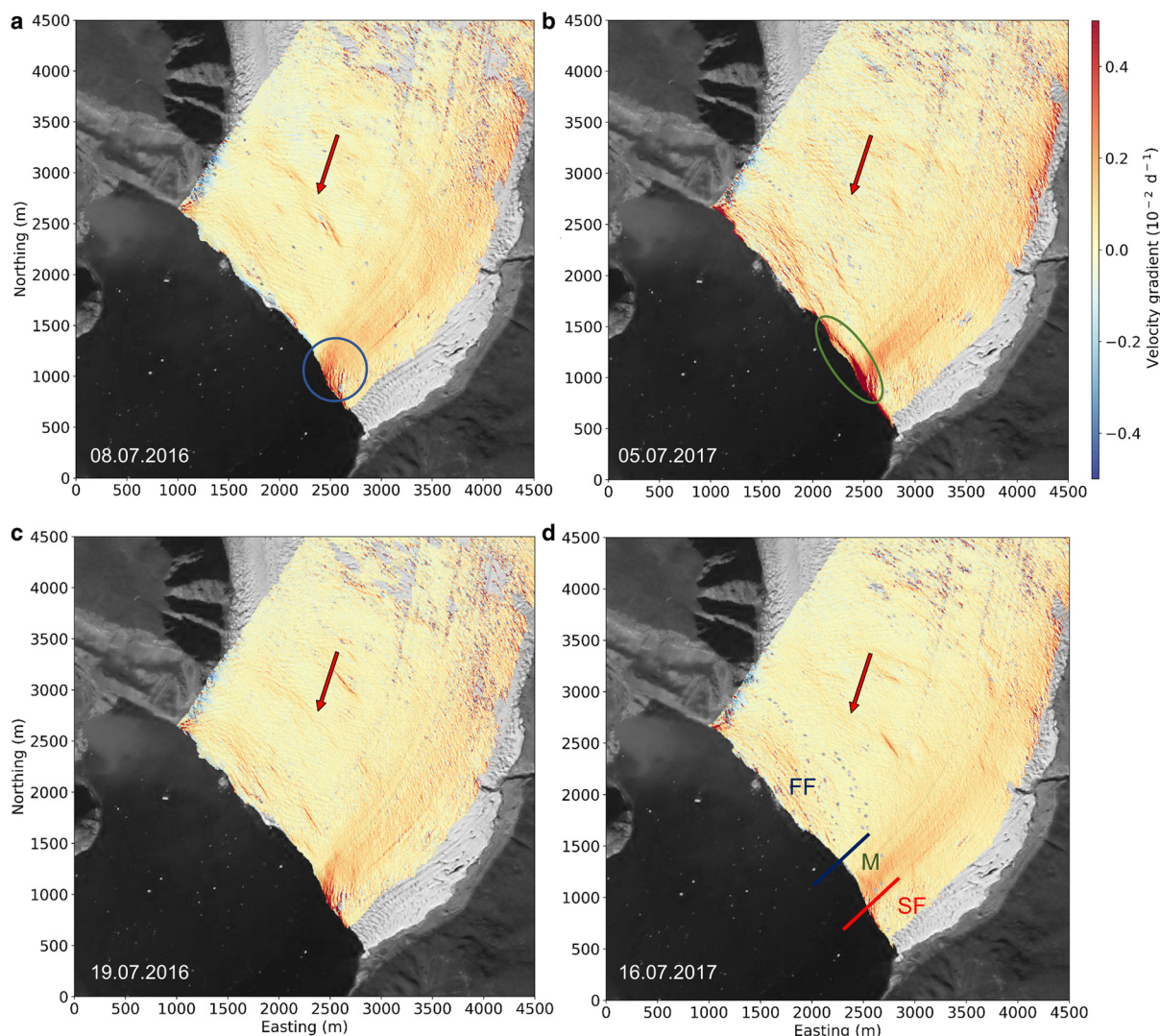
Fig. 10. Velocity gradient maps for Bowdoin Glacier (a) at the beginning and (c) at the end of the observation period in 2016 and (b) at the beginning and (d) at the end of the field campaign 2017. The blue circle shows a zone with high velocity gradients between the middle (M) and the slow-flowing sector (SF). The green circle marks the area calving off 3 d later. The different sectors of the fronts are marked with lines. Background: Sentinel-2A scene from 25 July 2017 (from ESA Copernicus Science Hub: https://scihub.copernicus.eu).

water with a terminus, which is close to floatation. Smaller and smoother velocity gradients leave the ice relatively intact, with crevasses mainly perpendicular to the flow direction (Fig. 10). The flow velocities, their gradients and the inferred crevasse opening are clearly modulated by the tides (Fig. 12; Fig. 6 in van Dongen and others, 2020). The calving frequency is two orders of magnitude lower at Bowdoin Glacier than at Eqip Sermia and the mass loss of the vertical calving front is dominated by sporadic large-scale calving events (Fig. 14).

5.1 Relations between front characteristics and bed geometry

Both glaciers show distinct patterns of terminus dynamics which can be related to their specific local topography. The smooth glacier surface of Bowdoin Glacier with homogeneous flow velocities with highest values in the centre and lower values towards the margins is related to a low surface slope and a simple U-shaped glacier valley without topographical steps (Fig. 4 in Sugiyama and others, 2015; Fig. 6 in Jouvet and others, 2017). At the transition of the almost stagnant area SF and sector M high velocity gradients (Fig. 10a) and crevasses tilted towards the flow direction were observed (marked area E in Fig. S1b). Using observations from repeated unmanned aerial vehicle (UAV) surveys and

modelling, Jouvet and others (2017) concluded that shallow bedrock at the southern margin causes reduced surface motion in sector SF and strong shearing in the marginal zone between the sectors SF and M.

Unlike Bowdoin Glacier, the terminus of Eqip Sermia is located on a very shallow bedrock ridge in sectors S and M (Fig. 10 in Lüthi and others, 2016), causing the formation of the current steep, inclined and very high calving front. The stress conditions of such a steep geometry cause bulging and extrusion (Hanson and Hooke, 2000; Leysinger-Vieli and Gudmundsson, 2004), which leads to the observed high longitudinal stresses and extensional strain rates causing faster flow at the terminus (Figs 4a, 9; Lüthi and others, 2016; Mercenier and others, 2018). The ice cliff was substantially lower and vertical in sector D where the fjord is deeper. Further upstream the glacier surface shows several steps in the steep slope (Fig. 9a), which lead to a highly crevassed surface and damaged ice flowing towards the front.

At Eqip Sermia the high spatial variability of glacier dynamics is influenced by small-scale variations of the bed topography, which cause the glacier velocity to vary non-uniformly along the front (Fig. 5a). It is remarkable how similar the flow velocities in the shallow sector S were in 2016 and 2017, whereas they changed strongly in sectors D and M between the campaigns (Fig. 5a).

Table 3. Number, event sizes and frequency of calving events of the TRI field campaigns at Eqip Sermia and Bowdoin Glacier

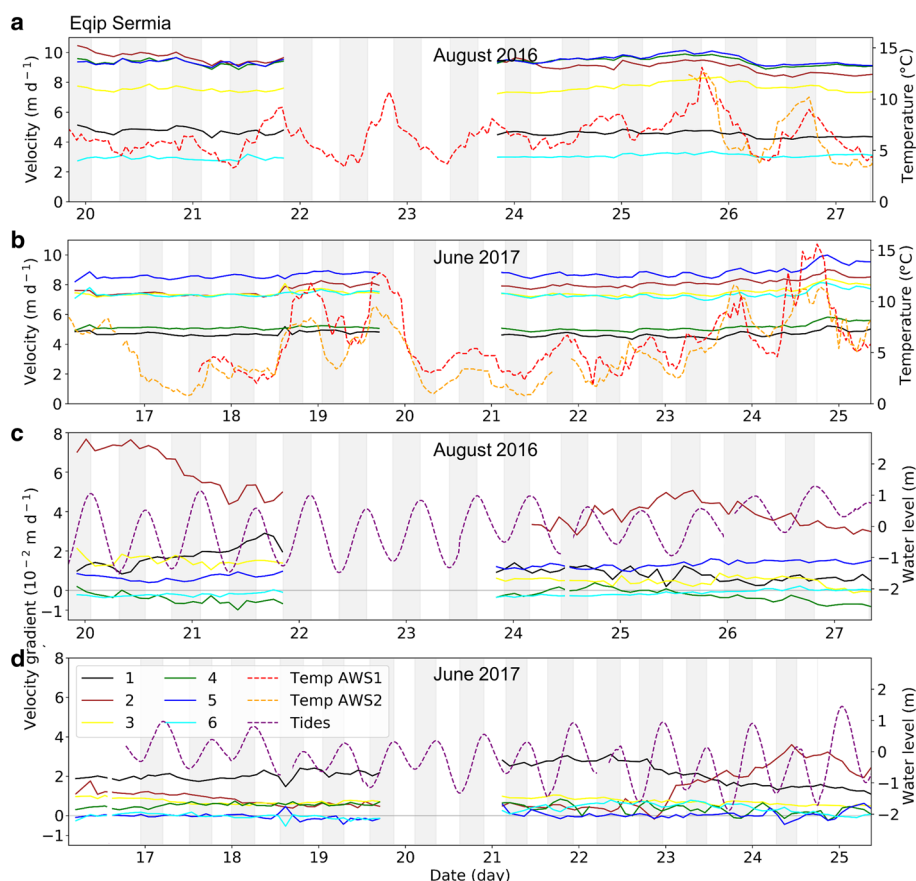|	Eqip Sermia 2016	Eqip Sermia 2017	Bowdoin 2016	Bowdoin 2017
Campaign duration (d)	6.1	8.6	11.9	9.8
Total event number	906	917	32	7
Event number per day	149	107	2.7	0.7
Total event volume (10^6 m^3)	16.0	17.4	0.2	0.9
Event volume per day (10^6 m^3)	2.6	2.0	0.02	0.09
Event sizes				
Mean (m^3)	17 700	19 000	7025	133 700
Maximum (m^3)	275 700	570 900	28 300	844 000
Minimum (m^3)	660	613	2020	3230

Fig. 11. Velocity at six points (Fig. 4a) along the front of Eqip Sermia over time for (a) 2016 and (b) 2017. The air temperature (dashed lines) of the two weather stations is shown on the right axis. The velocity gradient is shown for the same points over time for 2016 in (c) and for 2017 in (d). The grey background shading indicates rising tides. The tide measured with a pressure sensor in the fjord opposite of the glacier (dashed line) is shown on the right axis.

The relation of ice dynamics to the bedrock topography is exemplified in sector M. In 2016 the front was in a retreated position and the glacier rested on bedrock visible above water (purple box in Fig. 9a). Compared to 2017 this caused a higher and steeper front (Figs 5b, 7a) and consequently higher stresses which lead to positive velocity gradients (Fig. 9) and faster ice flow (Figs 4a, 5a, 8a). During the 2017 field season sector M was in an advanced position. The ice flow was characterised by a compressive zone with negative velocity gradients (Figs 9b, d) likely indicating a bedrock depression – a hypothesis supported by the circular crevasses in area C (indicated in Fig. S1a). At the same location plume P3 was observed (Fig. 13), which was usually the first plume forming every year (Kneib-Walter and others, 2021). It is likely that subglacial meltwater discharge is routed to deeper parts of the fjord (Shreve, 1972).

In general, our observations show how the bed and fjord topographies affect the geometry and dynamics of the glacier front. Complex undulating bed topographies induce large stresses and glacier dynamic variations at both glaciers, whereby shallow areas at Eqip Sermia produce high ice cliffs with high along flow velocity gradients. Glacier topography also affects crevassing, with topographic steps leading to higher damage and a smooth and flatter slope to more intact ice.

5.2 Sensitivity to air temperature and tides

Different bathymetry, flow characteristics and front geometries cause different sensitivities of glaciers to external forcings, such as tides and air temperatures. Major parts of the Bowdoin Glacier front are close to floatation with the fjord bottom 100–250 m below sea level (Fig. 6 in Jouvet and others, 2017; Fig. 4 in Sugiyama and others, 2015) and therefore are more exposed to oceanic forcing than Eqip Sermia. At Bowdoin Glacier a significant relationship between the tide rates and the velocity was observed. Figure 12 shows that highest velocities and extensional strain rates occurred at decreasing tides, suggested to be caused by the reduced water pressure on the calving front (Sugiyama and others, 2015). The semidiurnal variation of the velocity gradient
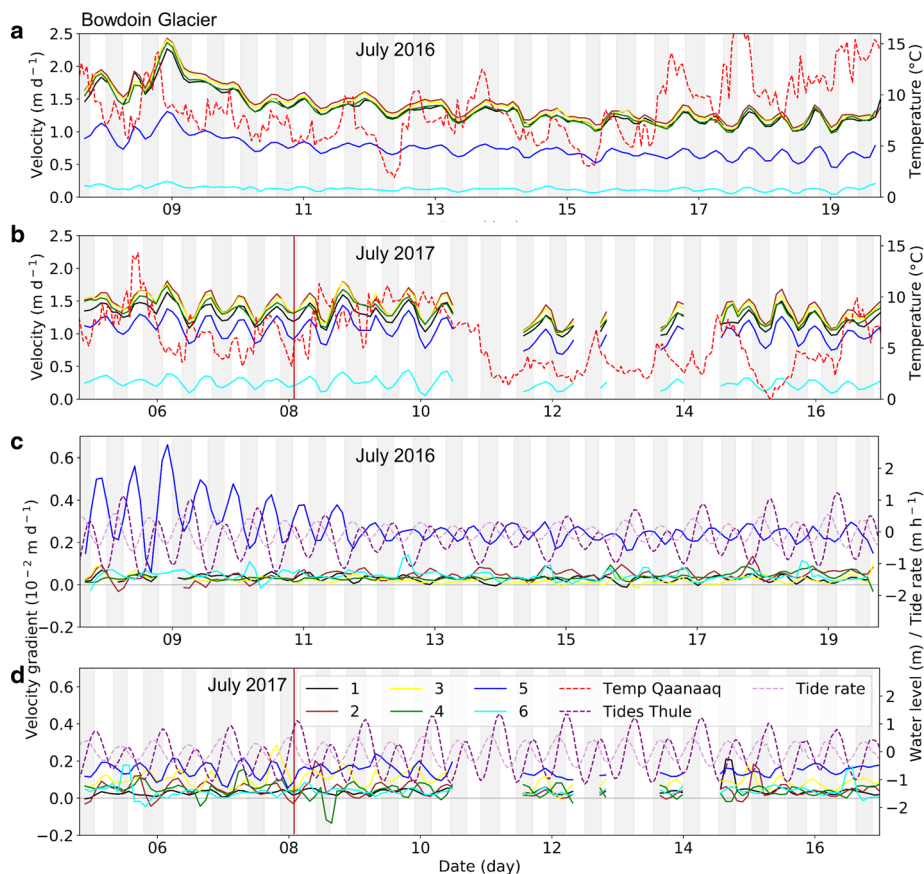
Fig. 12. Velocity at six points (Fig. 4b) along the front of Bowdoin Glacier over time for (a) 2016 and (b) 2017. The air temperature of the weather station in Qaanaaq is shown on the right axis. The velocity gradient is shown for the same points over time for (c) 2016 and (d) 2017. The grey background shading indicates rising tides. The tide measured in Thule (dashed line) is shown on the right axis together with the tide rate. The red vertical line indicates the timing of the large calving event observed in 2017.

induced by the tides, which is particularly well visible before the large calving event in 2017 (Fig. 14), leads to variations in the opening rate of the crevasses (Van Dongen and others, 2020). These variations in the longitudinal stretching of the glacier surface have also been observed to induce high levels of seismic activity at the glacier surface with falling tides (Podolskiy and others, 2016).

The relationship between the tides and velocity differs between the sectors. While sector M is very close to flotation and sector FF is only several metres above flotation, sector SF is estimated to be ~15 m above flotation (water depth values from Jouvet and others, 2017). This results in a weaker tidal response to velocity and the velocity gradient of point 6 and in a stronger response for the close to floatation sector M (point 5; Fig. 12).

A marked speed-up occurred at the beginning of the field campaign 2016 (Fig. 12a). The days before this speed-up were very warm (3 d with air temperatures above 10°C) and simultaneously the first meltwater plumes emerged at the calving front. This leads to the suggestion that the speed-up was caused by enhanced meltwater input to the base, which is consistent with the interpretation of enhanced basal motion based on UAV observations of the same event (Jouvet and others, 2018). A similar fast response to air temperature rise was also detected in 2013 and 2014 (Sugiyama and others, 2015). During the speed-up event an increasing velocity gradient at point 5 with strong tidal variations (Fig. 12c) was caused by higher shear at the margin between sectors M and SF as sector SF shows no clear acceleration (point 6 in Fig. 12b).

At Eqip Sermia the short-term forcing by air temperature and tides on the glacier dynamics is relatively weak in absolute terms. Indeed, when subtracting the mean velocity, temporal velocity variations of only a few decimetres per day become visible. Peaks in air temperatures cause in many occasions a slight acceleration in flow, especially in the field campaign 2017 (Fig. S2). The whole glacier is clearly grounded. Assuming a water depth

of 100 m (Lüthi and others, 2016) at sector D results in a height above flotation of 35–180 m. In 2017 the front in sector D was considerably lower and closest to floatation (20 m). During that time points 5 and 6 show a slight positive correlation between tide rate and velocity variation (more significant considering a short time lag of <1 h; Fig. S2), while this tidal response was absent at other points and during the field campaign 2016.

A slight increase of velocities is observed during the early melt season (end of field campaign 2017; Fig. 11b and Fig. S2b), which was also observed in other studies about Eqip Sermia and linked to enhanced basal motion (Lüthi and others, 2016; Kneib-Walter and others, 2021; Rohner and others, unpublished). The velocity gradient at point 2 next to the area with highest velocities increased simultaneously (Fig. 11d) indicating enhanced extension.

At the grounded Eqip Sermia a response to tides only occurs when the front position terminates in deeper water and variations caused by air temperature are small in absolute terms, compared to Bowdoin Glacier, which showed much stronger short-term variations resulting from tide and air temperature. These observations highlight how the sensibility of these two glaciers to external forcings are on different timescales (seasonal for Eqip Sermia, minutes to hours for Bowdoin Glacier) and of different magnitudes.

5.3 Calving activity and style

At Bowdoin Glacier the mass loss was dominated by a few large events of which one was captured in 2017 and small events during the rest of the time. This observation agrees with other studies at Bowdoin Glacier (Jouvet and others, 2017; Minowa and others, 2019) and Rink Isbræ, a major West Greenland outlet glacier (Medrzycka and others, 2016), where the mass loss was also dominated by a few large calving events. The large event in
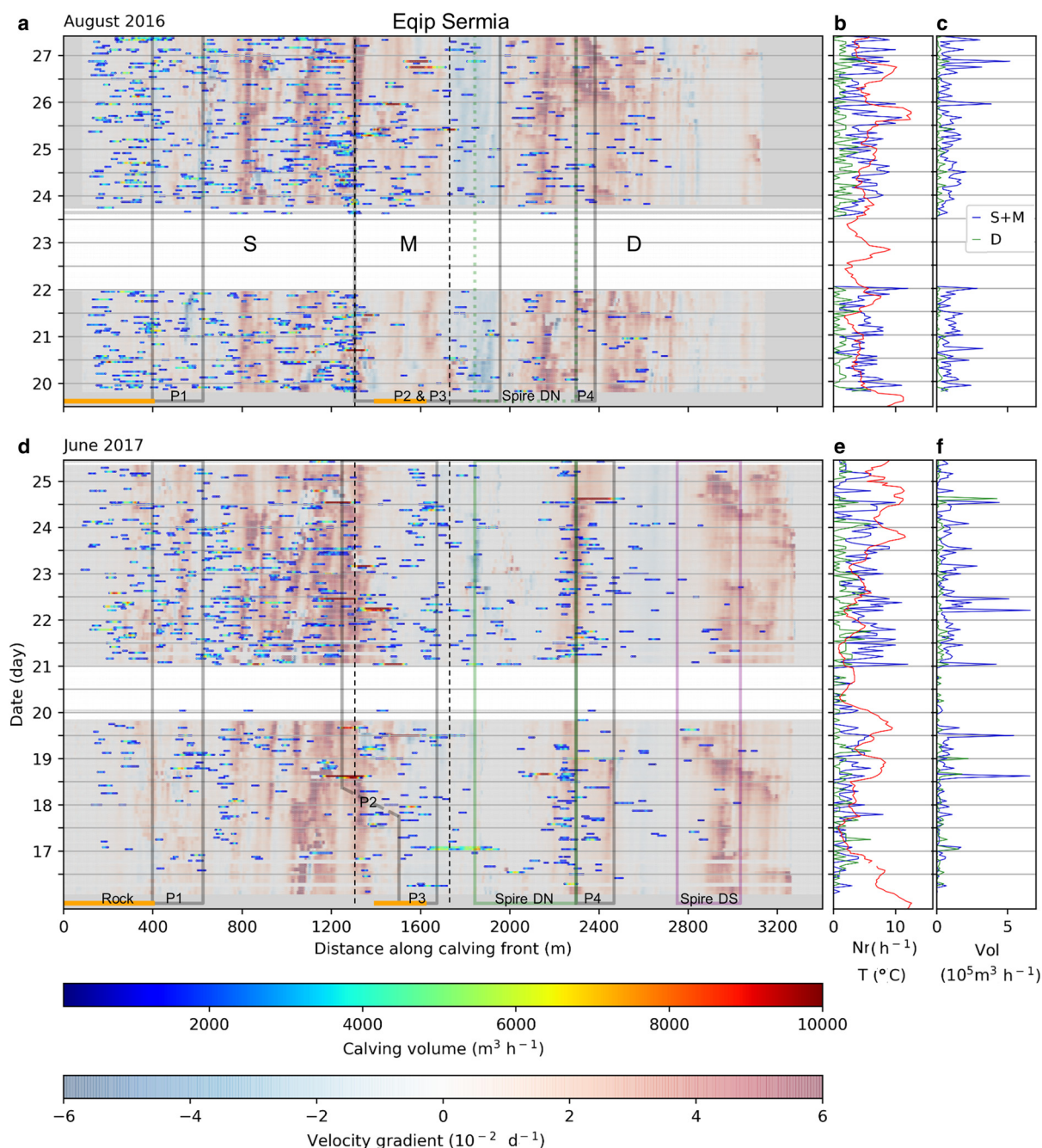
Fig. 13. Calving event volumes at Eqip Sermia along the front over time (a) for 2016 and (d) for 2017. Calving volumes sampled during 1 h intervals are colour coded. The background presents the velocity gradient along the front over time with positive values indicating extension (acceleration in downstream distance). White areas indicate data gaps. The orange horizontal bars at the bottom of (a) and (d) correspond to bedrock visible above the waterline. The grey boxes indicate the location and presence of meltwater plumes. Plumes P2, P3 and P4 can merge together. The black dotted vertical lines separate the sectors shallow (S), middle (M) and deep (D). The northern spire in sector D (DN) is indicated with a green box with a solid frame if the spire is still high and a dotted frame if the spire is in its low state (Walter and others, 2021). The southern spire in sector D (DS) is marked with a purple box. Number of events per hour over time and air temperature are shown in the middle panels for 2016 in (b) and 2017 in (e). The right panels show the volume of events per hour over time for (c) 2016 and (f) 2017. Number and volume of calving events per hour are separated into the shallow (blue line, together with the middle) and deep sector (green line).

2017 at Bowdoin Glacier occurred after the formation of a long crevasse opening parallel to the calving front likely caused by undercutting of the calving front by a meltwater plume and hydrofracturing due to a stream on the moraine (van Dongen and others, 2020). In the few days before the large calving event the TRI detected a clear increase in velocity gradient, which was tidally modulated (Fig. 14d). With the calving event the velocity gradient instantly dropped to very low levels. The crevasse causing the calving was initiated at the area with highest lateral shearing (Figs 10a and b; Jouvet and others, 2017). The smaller events detected in 2016 in sector SF were clustered in proximity to the

subglacial meltwater plume P1, which caused undercutting next to the high-shear zone, in accordance with time-lapse images and pressure sensor observations (Minowa and others, 2019). Minowa and others (2019) found for 2015 and 2016 a higher calving rate during periods with higher air temperatures and falling tides. Such a relation was not observed in our data, likely due to inability of the TRI to detect small event sizes. No retreat and advance of the calving front during the observation period was observed suggesting that the front ablation and the mass flux of the glacier are of comparable magnitude. However a rough estimation of the mass flux leads to $600\,000\,\mathrm{m}^3$ ice per
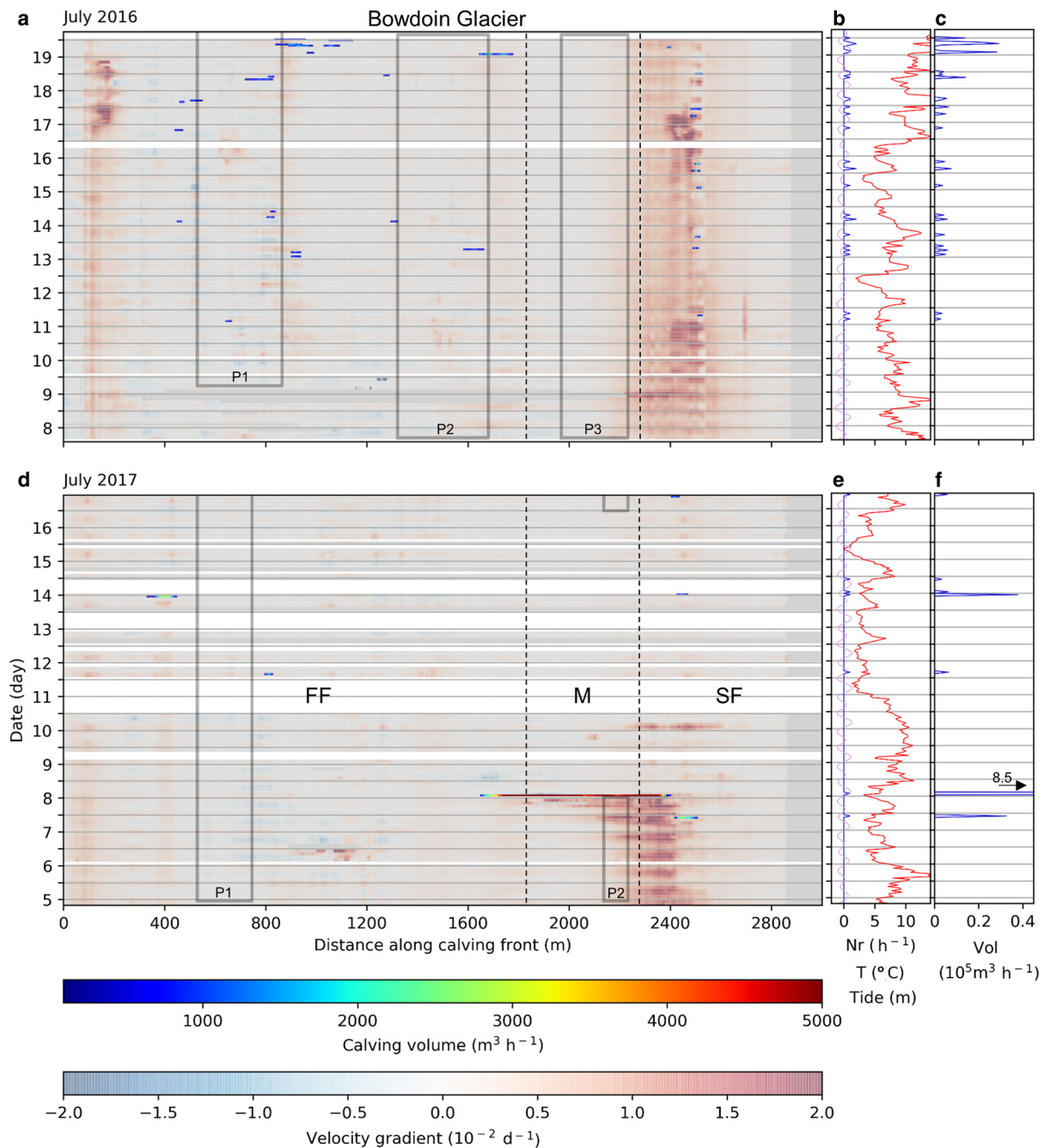
Fig. 14. Calving event volumes at Bowdoin Glacier along the front over time (a) for 2016 and (d) for 2017. Calving volumes sampled during 1 h intervals are colour coded. The background presents the velocity gradient along the front over time with positive values indicating extensional forces. The velocity gradient shows a clear tidal signal. White areas indicate data gaps. The grey boxes indicate the location and presence of meltwater plumes. The black dotted vertical lines separate the sectors fast flowing (FF), middle (M) and slow flowing (SF). Number of events per hour over time, air temperature and tides are shown in the middle panels for 2016 in (b) and 2017 in (e). The right panels show the volume of events per hour over time for (c) 2016 and (f) 2017.

day, which is considerably larger than the calving volume per day detected with the TRI (30 times larger in 2016, 7 times larger in 2017). Thus, even if small events not detectable with the TRI are considered, oceanic melt is likely an important process for Bowdoin Glacier, which was also concluded in other studies based on different observations (Jouvet and others, 2018; Minowa and others, 2019).

In contrast, Eqip Sermia was characterised by smaller but much more frequent calving events with a seasonal pattern influenced by the ice melange breakup, the bedrock topography and subglacial meltwater plumes leading to undercutting of the calving front (Kneib-Walter and others, 2021). Large-size calving events similar to those observed at Bowdoin Glacier could not be detected on hourly/daily time-lapse images from 2014 to

2019 (Kneib-Walter and others, 2021). The observations in 2016 and 2017 showed a very distinct calving frequency and pattern, which can be explained by the calving front being at a different state in the seasonal cycle. In the early melt season (field campaign 2017) large events occurred where subglacial meltwater plumes emerged at the surface. At this location the front retreated during the observation period. Later in the melt season (field campaign 2016) the three sectors showed a distinct pattern caused by the different front geometries and processes, with reduced calving activity in sector D due to substantial subaquatic calving and oceanic melt (Walter and others, 2020).

At Eqip Sermia no strong relation between velocity gradients and calving events was detected, while at Bowdoin Glacier the velocity gradient clearly increases before the large calving event in

2017. This is likely due to the already highly damaged and crevassed ice of the very high and steep front of Eqip Sermia leading to frequent and smaller-sized calving. This hypothesis is supported by the observation of larger events following an increase in velocity gradient mainly in the early melt season (e.g. 2017), when the crevasses are less pronounced than later in the season (Kneib-Walter and others, 2021).

The highly damaged ice of Eqip Sermia is likely also the explanation why the deeper sector D with a similar front geometry as Bowdoin Glacier is characterised by more frequent and smaller calving events and not by sporadic large-scale events.

Observations at other highly crevassed glaciers of similar size than Eqip Sermia, like Yahtse Glacier in Alaska (Bartholomaus and others, 2015; Durkin and others, 2017), Kronebreen (Chapuis and others, 2014) and Store Glacier (Cook and others, 2021) agree with the suggestion that highly damaged ice causes frequent, smaller size calving instead of large-scale calving events. The ice flow of Yahtse Glacier and Store Glacier is also influenced by topographical steps, likely increasing the crevasse intensity.

The different front geometries and dominating processes affecting these glaciers produce a variety of different calving styles controlled by different types of calving mechanisms. At Bowdoin Glacier the large calving event in 2017 can be related to stress concentrations caused by a bed bump, while at Eqip Sermia a relation between velocity gradient and calving was only found in the early melt season, when the surface is less crevassed and large calving events can occur. The high density of deep crevasses advected towards the calving front provides many nucleation sites for small-scale break-off events, which than release icebergs. The calving activity and style can change over time, when the dominating processes are altered by the evolving terminus geometry.

5.4 Implications for calving models

Current parametrisations of glacier calving rates, which are used in many large-scale ice-sheet models, are formulated in terms of a few extensive quantities, such as water depth and ice thickness at the terminus (e.g. Brown and others, 1982; Van der Veen, 1996; Vieli and others, 2001). In contrast, our measurements have demonstrated that frequency and volumes of calving are emerging properties that are controlled mainly by a combination of quantities and state variables such as the local stress field, the local bedrock topography, the amount, orientation and size of cracks and fractures and the intensity of melt by advection of warm ocean-bottom water. These quantities are controlled by the local geometry, the flow history and the seasonal evolution of the terminus. The same quantities in turn contribute to the evolution of the terminus geometry. This observational evidence shows that simple calving relations considering only one forcing, like for example water depth, are not able to reproduce the full complexity of the calving process.

There are several modelling approaches aiming at reproducing the emergent observed geometry and calving rates. Purely finite-element based approaches (e.g. Mercenier and others, 2019), purely particle dynamics models (e.g. Wolper and others, 2021) and combined approaches (e.g. Benn and others, 2017; Todd and others, 2018; Vallot and others, 2018) are currently used to understand the variety of emergent behaviour, the sensitivity to the choice of model parameters, and ranges of model parameters that lead to realistic terminus geometries and calving rates. These approaches are computationally expensive, and a main difficulty is the calibration of model parameters, which requires detailed and comprehensive datasets on glacier geometry, calving event sizes and timing and external forcings. As demonstrated in this study, an important aspect is the diversity of responses among different sectors of a single calving front, and

the largely different responses at different glaciers of similar size and characteristics. Additionally, observations that lack the context of the recurring seasonal evolution are of limited usefulness (Kneib-Walter and others, 2021). Detailed observations, such as those presented in this study, are essential to calibrate and validate the mentioned modelling approaches, which is essential to improve the calving representation in larger-scale ice dynamic models used to predict sea level rise.

6. Conclusion

Eqip Sermia and Bowdoin Glacier, two tidewater glaciers of the Greenland ice sheet with comparable dimensions but differing geometries, dynamics and calving patterns, were investigated with detailed field measurements in 2016 and 2017. At both glaciers a TRI was installed and the resulting measurements were used to analyse calving volume and frequency, calving front elevations, velocities and velocity gradients. These unique datasets enable us to investigate the impact of external forcings like tides and air temperature on the glacier dynamics and allow us to highlight the dominant factors explaining the shape and dynamic behaviour of the two glaciers. Such a comparison of the same measurements including calving and strain rates measured with a high spatial coverage and resolution of two glaciers of similar dimensions provides new insights into the complexity of calving glaciers.

When the ice flow is driven by a steep surface slope with several topographic steps, such as at Eqip Sermia, the flow velocities are high and the velocity gradient pattern is strongly heterogeneous. The observed patches of strongly extensional flow lead to a highly crevassed and damaged surface. On the other hand, a smooth and low surface slope, such as at Bowdoin Glacier, leads to lower velocities and smoother velocity gradients resulting in relatively intact ice. These resulting differences in crevasse intensity and extensional strain rate patterns explain the different calving patterns. While for a terminus with mostly intact ice the mass loss is dominated by sporadic large-scale calving events initiating in areas of high extension and stresses, a highly crevassed terminus leads to frequent and mostly smaller calving events, independent of the local velocity gradients.

Subglacial meltwater plumes are known to lead to faster and further terminus retreat due to undercutting of the calving front (Kneib-Walter and others, 2021). We find that for highly damaged ice, subglacial meltwater plumes are not influencing the calving pattern, whereas for less damaged ice, undercutting is expected to increase stresses and cause large-scale calving events.

The floatation level influences how a glacier reacts to short-term external forcings. A glacier close to floatation, such as at Bowdoin Glacier, shows a clear tidal response in both velocity and velocity gradient. Highest velocities and extensional strain rates occur at decreasing tides and are caused by the reduced water pressure on the calving front. High meltwater input can additionally lead to short-term speed-up events. On the other hand, a clearly grounded, fast flowing calving front, such as Eqip Sermia, shows no tidal response and the short-term reaction to air temperature is relatively weak in absolute terms.

The results also reveal the importance of the bed and fjord topography on the geometry and longer-term dynamics of the glacier front. A sharp transition towards a shallower area causes a change in velocity and consequently a stress concentration, which can become an initiation zone of large crevasses. Longitudinal underwater ridges with shallow water lead to further advance of the glacier front and the formation of high ice cliffs with high velocity gradients.

Our detailed observations demonstrate that both glaciers, and even their individual sectors, react to external forcings over timescales of hours to seasonal and at different magnitudes. The sensitivity of individual calving front sectors depends on the local geometry, which in term affects the local stress conditions. Highly damaged ice is less sensible to short-time external forcings as are clearly grounded calving fronts. The findings explain why similar glaciers show a different reaction to external forcing, which is important in view of performing prognostic modelling. The observed high heterogeneity of calving patterns and styles and the highlighted complexity of the interaction between the individual forcings require calving models to include for all underlying mechanisms and key drivers active at the investigated glaciers. To calibrate currently used numerical models, detailed and comprehensive datasets, like those presented in this study, on glacier geometry, calving and external forcings including theirs evolution throughout the seasonal cycle are required.

References

Bartholomaus TC and 5 others (2015) Tidal and seasonal variations in calving flux observed with passive seismology. *Journal of Geophysical Research: Earth Surface* **120**(11), 2318–2337. doi: 10.1002/2015JF003641

Benn D and 7 others (2017) Melt-under-cutting and buoyancy-driven calving from tidewater glaciers: new insights from discrete element and continuum model simulations. *Journal of Glaciology* **63**(240), 691–702. doi: 10.1017/jog.2017.41

Brown CS, Meier MF and Post A (1982) Calving Speed of Alaska Tidewater Glaciers, with Application to Columbia Glacier. *US Geological Survey Professional Paper* 1258-C, C1-C13, 4 sheets. Available at https://dggs.alaska.gov/pubs/id/4000, 21.06.2022.

Caduff R, Schlunegger F, Kos A and Wiesmann A (2015) A review of terrestrial radar interferometry for measuring surface change in the geosciences. *Earth Surface Processes and Landforms* **40**(2), 208–228. doi: 10.1002/esp. 3656

Cassotto R and 6 others (2019) Non-linear glacier response to calving events, Jakobshavn Isbræ, Greenland. *Journal of Glaciology* **65**(249), 39–54. doi: 10.1017/jog.2018.90

Chapuis A and Tetzlaff T (2014) The variability of tidewater-glacier calving: origin of event-size and interval distributions. *Journal of Glaciology* **60**(222), 622–634. doi: 10.3189/2014JoG13J215

Cook S, Christoffersen P, Truffer M, Chudley TR and Abellan A (2021) Calving of a large Greenlandic tidewater glacier has complex links to meltwater plumes and mélange. *Journal of Geophysical Research: Earth Surface* **126**(4), e2020JF006051. doi: 10.1029/2020JF006051

Davis J, De Juan J, Nettles M, Elosegui P and Andersen M (2014) Evidence for non-tidal diurnal velocity variations of Helheim Glacier, East Greenland. *Journal of Glaciology* **60**(224), 1169–1180. doi: 10.3189/2014JoG13J230

Durkin WJ, Bartholomaus TC, Willis MJ and Pritchard ME (2017) Dynamic changes at Yahtse Glacier, the most rapidly advancing tidewater glacier in Alaska. *Frontiers in Earth Science* **5**, 21. doi: 10.3389/feart.2017.00021

Enderlin EM and 5 others (2014) An improved mass budget for the Greenland ice sheet. *Geophysical Research Letters* **41**(3), 866–872. doi: 10.1002/2013GL059010

Fried MJ and 6 others (2018) Reconciling drivers of seasonal terminus advance and retreat at 13 central west Greenland tidewater glaciers. *Journal of Geophysical Research: Earth Surface* **123**(7), 1590–1607. doi: 10.1029/2018JF004628

Goldstein R (1995) Atmospheric limitations to repeat-track radar interferometry. *Geophysical Research Letters* **22**(18), 2517–2520. doi: 10.1029/95GL02475

Hanson B and Hooke RL (2000) Glacier calving: a numerical model of forces in the calving-speed/water-depth relation. *Journal of Glaciology* **46**(153), 188–196. doi: 10.3189/172756500781832792

Howat IM, Box JE, Ahn Y, Herrington A and McFadden EM (2010) Seasonal variability in the dynamics of marine-terminating outlet glaciers in Greenland. *Journal of Glaciology* **56**(198), 601–613. doi: 10.3189/002214310793146232

Howat IM, Joughin I, Fahnestock M, Smith BE and Scambos TA (2008) Synchronous retreat and acceleration of southeast Greenland outlet glaciers 2000–06. Ice dynamics and coupling to climate. *Journal of Glaciology* **54**(187), 646–660. doi: 10.3189/002214308786570908

The IMBIE Team (2020) Mass balance of the Greenland ice sheet from 1992 to 2018. *Nature* **579**, 233–239. doi: 10.1038/s41586-019-1855-2

Jouvet G and 7 others (2017) Initiation of a major calving event on the Bowdoin Glacier captured by UAV photogrammetry. *The Cryosphere* **11**(2), 911–921. doi: 10.5194/tc-11-911-2017

Jouvet G and 6 others (2018) Short-lived ice speed-up and plume water flow captured by a VTOL UAV give insights into subglacial hydrological system of Bowdoin Glacier. *Remote Sensing of Environment* **217**(2018), 389–399. doi: 10.1016/j.rse.2018.08.027

Kane E and 6 others (2020) Impact of calving dynamics on Kangilernata Sermia, Greenland. *Geophysical Research Letters* **47**(20), e2020GL088524. doi: 10.1029/2020GL088524

King MD and 8 others (2020) Dynamic ice loss from the Greenland ice sheet driven by sustained glacier retreat. *Nature Communications Earth & Environment* **1**(1), 233. doi: 10.1038/s43247-020-0001-2

Kneib-Walter A, Lüthi MP, Moreau L and Vieli A (2021) Drivers of recurring seasonal cycle of glacier calving styles and patterns. *Frontiers in Earth Science* **9**, 667717. doi: 10.3389/feart.2021.667717

Leysinger-Vieli GJ-MC and Gudmundsson GH (2004) On estimating length fluctuations of glaciers caused by changes in climatic forcing. *Journal of Geophysical Research: Earth Surface* **109**(F1), F01007. doi: 10.1029/2003JF000027

Lüthi MP and 6 others (2016) A century of geometry and velocity evolution at Eqip Sermia, West Greenland. *Journal of Glaciology* **62**(234), 640–654. doi: 10.1017/jog.2016.38

Lüthi MP and Vieli A (2016) Multi-method observation and analysis of a tsunami caused by glacier calving. *The Cryosphere* **10**(3), 995–1002. doi: 10.5194/tc-10-995-2016

Medrzycka D, Benn DI, Box JE, Copland L and Balog J (2016) Calving behavior at Rink Isbræ, West Greenland, from time-lapse photos. *Arctic, Antarctic, and Alpine Research* **48**(2), 263–277. doi: 10.1657/AAAR0015-059

Mercenier R, Lüthi MP and Vieli A (2018) Calving relation for tidewater glaciers based on detailed stress field analysis. *The Cryosphere* **12**(2), 721–739. doi: 10.5194/tc-12-721-2018

Mercenier R, Lüthi MP and Vieli A (2019) A transient coupled ice flow-damage model to simulate iceberg calving from tidewater outlet glaciers. *Journal of Advances in Modeling Earth Systems* **11**(9), 3057–3072. doi: 10.1029/2018MS001567

Minowa M and 5 others (2019) Calving flux estimation from tsunami waves. *Earth and Planetary Science Letters* **515**(2019), 283–290. doi: 10.1016/j.epsl.2019.03.023

Moon T, Joughin I, Smith B and Howat I (2012) 21st-century evolution of Greenland outlet glacier velocities. *Science* **336**(6081), 576–578. doi: 10.1126/science.1219985

Podolskiy EA and 7 others (2016) Tide-modulated ice flow variations drive seismicity near the calving front of Bowdoin Glacier, Greenland. *Geophysical Research Letters* **43**(5), 2036–2044. doi: 10.1002/2016GL067743

Podrasky D and 5 others (2012) Outlet glacier response to forcing over hourly to interannual timescales, Jakobshavn Isbræ, Greenland. *Journal of Glaciology* **58**(212), 1212–1226. doi: 10.3189/2012JoG12J065

Rignot E, Fenty I, Xu Y, Cai C and Kemp C (2015) Undercutting of marine terminating glaciers in West Greenland. *Geophysical Research Letters* **42**(14), 5909–5917. doi: 10.1002/2015GL064236

Rignot E and Kanagaratnam P (2006) Changes in the velocity structure of the Greenland Ice Sheet. *Science* **311**(5763), 986–990. doi: 10.1126/science.1121381

Sakakibara D and Sugiyama S (2018) Ice front and flow speed variations of marine-terminating outlet glaciers along the coast of Prudhoe Land, northwestern Greenland. *Journal of Glaciology* **64**(244), 300–310. doi: 10.1017/jog.2018.20

Sakakibara D and Sugiyama S (2020) Seasonal ice-speed variations in 10 marine-terminating outlet glaciers along the coast of Prudhoe Land, northwestern Greenland. *Journal of Glaciology* **66**(255), 25–34. doi: 10.1017/jog.2019.81

Schild KM and Hamilton GS (2013) Seasonal variations of outlet glacier terminus position in Greenland. *Journal of Glaciology* **59**(216), 759–770. doi: 10.3189/2013JoG12J238

Seddik H and 5 others (2019) Response of the flow dynamics of Bowdoin Glacier, northwestern Greenland, to basal lubrication and tidal forcing. *Journal of Glaciology* **65**(250), 225–238. doi: 10.1017/jog.2018.106

Shreve RL (1972) Water movement in glaciers. *Journal of Glaciology* **11**(62), 205–214. doi: 10.3189/S002214300002219X

Strozzi T, Werner C, Wiesmann A and Wegmüller U (2012) Topography mapping with a portable real-aperture radar interferometer. *IEEE Geoscience and Remote Sensing Letters* **9**(2), 277–281. doi: 10.1109/LGRS.2011.2166751

Sugiyama S, Sakakibara D, Tsutaki S, Maruyama M and Sawagaki T (2015) Glacier dynamics near the calving front of Bowdoin Glacier, Northwestern Greenland. *Journal of Glaciology* **61**(226), 223–232. doi: 10.3189/2015JoG14J127

Sundal AV and 5 others (2013) Controls on short-term variations in Greenland glacier dynamics. *Journal of Glaciology* **59**(217), 883–892. doi: 10.3189/2013JoG13J019

Todd J and 10 others (2018) A full-Stokes 3-D calving model applied to a large Greenlandic Glacier. *Journal of Geophysical Research: Earth Surface* **123**(3), 410–432. doi: 10.1002/2017JF004349

Tsutaki S, Sugiyama S, Sakakibara D and Sawagaki T (2016) Surface elevation changes during 2007–13 on Bowdoin and Tugto Glaciers, northwestern Greenland. *Journal of Glaciology* **62**(236), 1083–1092. doi: 10.1017/jog.2016.106

Vallot D and 9 others (2018) Effects of undercutting and sliding on calving: a global approach applied to Kronebreen, Svalbard. *The Cryosphere* **12**(2), 609–625. doi: 10.5194/tc-12-609-2018

van den Broeke MR and 7 others (2016) On the recent contribution of the Greenland ice sheet to sea level change. *The Cryosphere* **10**(5), 1933–1946. doi: 10.5194/tc-10-1933-2016

Van der Veen CJ (1996) Tidewater calving. *Journal of Glaciology* **42**(141), 375–385. doi: 10.3189/S0022143000004226

van Dongen E and 8 others (2020) Tides modulate crevasse opening prior to a major calving event at Bowdoin Glacier, Northwest Greenland. *Journal of Glaciology* **66**(255), 113–123. doi: 10.1017/jog.2019.89

van Dongen E and 10 others (2021) Thinning leads to calving-style changes at Bowdoin Glacier, Greenland. *The Cryosphere* **15**(2), 485–500. doi: 10.5194/tc-15-485-2021

Vieli A, Funk M and Blatter H (2001) Flow dynamics of tidewater glaciers: a numerical modelling approach. *Journal of Glaciology* **47**(159), 595–606. doi: 10.3189/172756501781831747

Vieli A, Jania J, Blatter H and Funk M (2004) Short-term velocity variations on Hansbreen, a tidewater glacier in Spitsbergen. *Journal of Glaciology* **50**(170), 389–398. doi: 10.3189/172756504781829963

Voytenko D and 5 others (2015) Tidally driven ice speed variation at Helheim Glacier, Greenland, observed with terrestrial radar interferometry. *Journal of Glaciology* **61**(226), 301–308. doi: 10.3189/2015JoG14J173

Walter A, Lüthi MP and Vieli A (2020) Calving event size measurements and statistics of Eqip Sermia, Greenland, from terrestrial radar interferometry. *The Cryosphere* **14**(3), 1051–1066. doi: 10.5194/tc-14-1051-2020

Werner C, Strozzi T, Wiesmann A and Wegmüller U (2008a) A Real aperture radar for ground-based differential interferometry. *IGARSS 2008 – 2008 IEEE International Geoscience and Remote Sensing Symposium* 2008, III-210–III-213. doi: 10.1109/IGARSS.2008.4779320

Werner C, Wiesmann A, Strozzi T and Wegmüller U (2008b) Gamma's portable radar interferometer, 13th FIG International Symposium on Deformation Measurement and Analysis, Lisbon, Portugal, May 12–15, 1–10. Available at https://www.fig.net/resources/proceedings/2008/lisbon_2008_comm6/papers/ps02/ps02_04_werner_mc016.pdf (21.06.2022).

Wolper J and 6 others (2021) A glacier–ocean interaction model for tsunami genesis due to iceberg calving. *Nature Communication Earth & Environment* **2**, 130. doi: 10.1038/s43247-021-00179-7

Xie S, Dixon TH, Holland DM, Voytenko D and Vanková I (2019) Rapid iceberg calving following removal of tightly packed proglacial mélange. *Nature Communications* **10**, 3250. doi: 10.1038/s41467-019-10908-4

Xie S, Dixon TH, Voytenko D, Deng F and Holland DM (2018) Grounding line migration through the calving season at Jakobshavn Isbræ, Greenland, observed with terrestrial radar interferometry. *The Cryosphere* **12**(4), 1387–1400. doi: 10.5194/tc-12-1387-2018